Chapter 9
Imaging Dynamics of Femtosecond Laser-Induced Surface Nanostructuring

Cong Cong, Ranran Fang, Anatoliy Y. Vorobyev, Mohamed ElKabbash, Subhash C. Singh, and Chunlei Guo

Abstract Over the past years, direct femtosecond laser surface processing has distinguished itself from other conventional laser ablation methods and becomes an important method to create surface structures at nano- and microscales due to its flexibility, simplicity, and controllability in creating various types of nano-/microstructures that are suitable for a wide range of applications. Significant advancements were made recently in applying this technique to altering optical properties of metals and semiconductors, such as highly absorptive or novel materials with wetting properties ranging from superhydrophilic to superhydrophobic.

To explore the dynamics of surface nanostructuring, here we describe some recent progresses on a scattered-light-based optical imaging technique which allows the capture of the complete temporal and spatial evolution of the femtosecond laser-induced morphological surface structural dynamics of metals from start to finish, that is, from the initial transient surface fluctuations, through melting and ablation, to the end of resolidification.

The formation dynamics of the surface structures at different length scales and the sequence of their appearance changes with laser fluence are discussed. The mechanisms driving each of these dynamic steps are discussed.

Keywords Ultrafast dynamics · Imaging · Nanostructuring · Transient surface structure

1 Introduction of Nanostructuring

Surface morphology plays a key role in determining the optical, mechanical, wetting, chemical, biological, and other properties of a solid surface. Recently, femtosecond laser surface nanostructuring has emerged as a novel and versatile

C. Cong · R. Fang · A. Y. Vorobyev · M. ElKabbash · S. C. Singh · C. Guo (✉)
The Institute of Optics, University of Rochester, Rochester, NY, USA
e-mail: ccong@ur.rochester.edu; anatoliy.vorobyev@rochester.edu; mke23@case.edu; ssingh49@UR.Rochester.edu; chunlei.guo@rochester.edu

R. Stoian, J. Bonse (eds.), *Ultrafast Laser Nanostructuring*, Springer Series in Optical Sciences 239, https://doi.org/10.1007/978-3-031-14752-4_9

way for producing a large variety of surface nanostructures enabling a wide range of applications in photonics, plasmonics, optoelectronics, biochemical sensing, micro/nano-fluidics, optofluidic, biomedicine, and other areas [1]. The advantages of femtosecond laser surface patterning include ability of processing nearly all types of materials (metals, semiconductors, glasses, and polymers), capability of processing nonplanar surfaces, ability of producing nanostructures on surface areas from nanoscale to macroscale, and maskless single-step processing at a high speed under normal ambient conditions, without needing a clean room environment [2, 3].

With the advent of femtosecond lasers, the potential for femtosecond lasers in ablation-based micro- and nano-processing has been demonstrated [1, 4–7]. Initially, a number of techniques using femtosecond lasers assisted by other techniques were developed for surface nanostructuring and nanopatterning of solids, such as near-field nanomachining [8], laser-assisted chemical etching [9], and deposition from femtosecond laser-ablated plumes [10]. It was also found that laser-induced periodic surface structures that had previously been generated using long-pulsed lasers can also be produced by femtosecond laser pulses on nearly all types of materials, including semiconductors [11–14], dielectrics [2, 3, 15], and metals [16–18]. More recently, direct femtosecond laser processing stood out as a new field for surface nanostructuring and nanopatterning due to its flexibility, simplicity, and capability of producing a large variety of surface structures suitable for a wide range of application [1, 6]. Figure 9.1 shows some typical nano- and microscale images following femtosecond laser irradiation [6].

With the development of femtosecond laser nanostructuring, novel materials have been created such as black silicon [9], black and colored metals [16, 19, 20], colored silicon [21], and materials with strong hydrophobicity [7, 22–24], hydrophilicity [25] and even with the extreme of liquid-transporting superwicking effect [26, 27]. Figure 9.2 shows some typical laser-processed material: colored metals [1], superhydrophilic surface [6], and superhydrophobic surface [7]. Furthermore, it has been demonstrated that the femtosecond laser-induced surface structures can be successfully used for significant enhancement of X-ray generation [28], photoelectron emission [29], and thermal radiation from incandescent light sources [30]. Biological applications have also been explored with surface nanopatterning [31–33].

2 Selected Ultrafast Imaging Methods

To explore the dynamics process of nanostructuring, time-resolved imaging techniques are required. Ultrafast morphological and crystalline structural dynamics have been studied using various techniques, including optical imaging [34–40], X-ray diffraction [41, 42], electron diffraction [43], and diffractive XUV imaging [44].

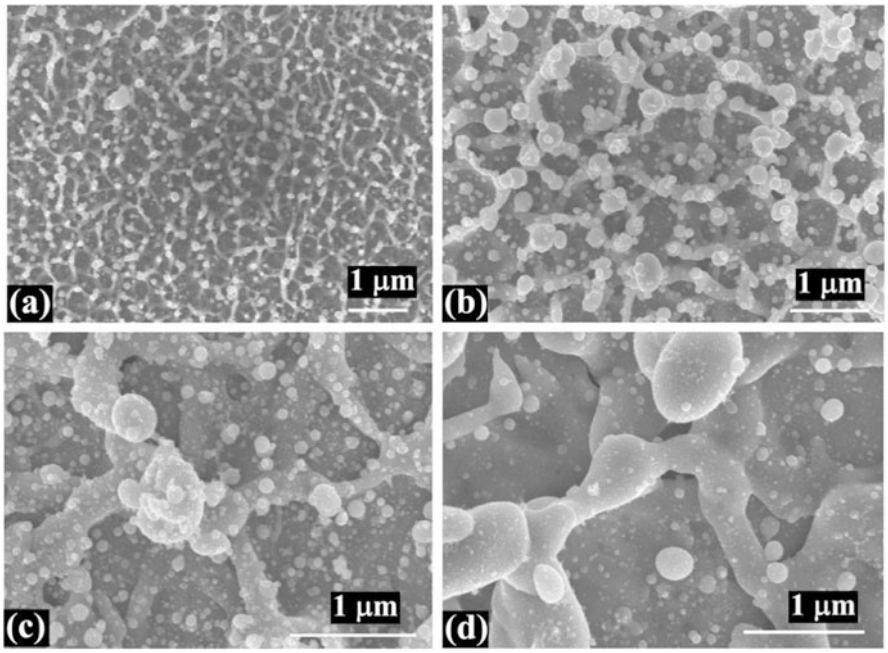

Fig. 9.1 Typical nano- and microscale images following direct femtosecond laser processing. SEM images of irradiated copper following ablation (**a**) after 1 shot featuring only random nanostructures in the form of nanoprotrusions and nanocavities, (**b**) surface after 2 shots featuring only random nanostructures in the form of spherical nanoprotrusions and nanocavities, (**c**) surface after 10 shots featuring both nano- and microstructures, and (**d**) surface after 1000 shots showing microstructures being dominating. (Reprinted with permission from Ref. [6])

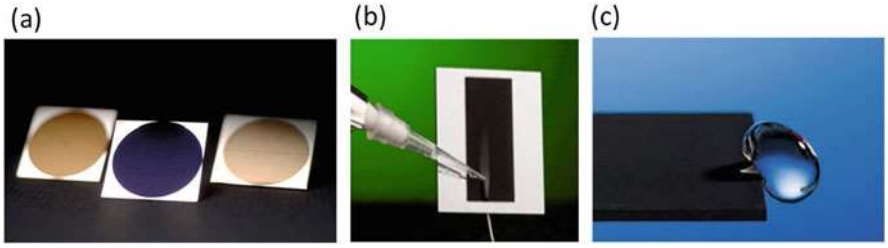

Fig. 9.2 Femtosecond laser produced (**a**) colored metals [1], (**b**) superhydrophilic surface [6], and (**c**) superhydrophobic surface [7]

2.1 Ultrafast Optical Imaging

Optical imaging can be achieved by collecting specular reflections [34–40], which is more suitable for resolving relatively large changes in reflection, such as formation of Newton rings [35–39]. K. Sokolowski-Tinten et al. used a pump pulse to excite

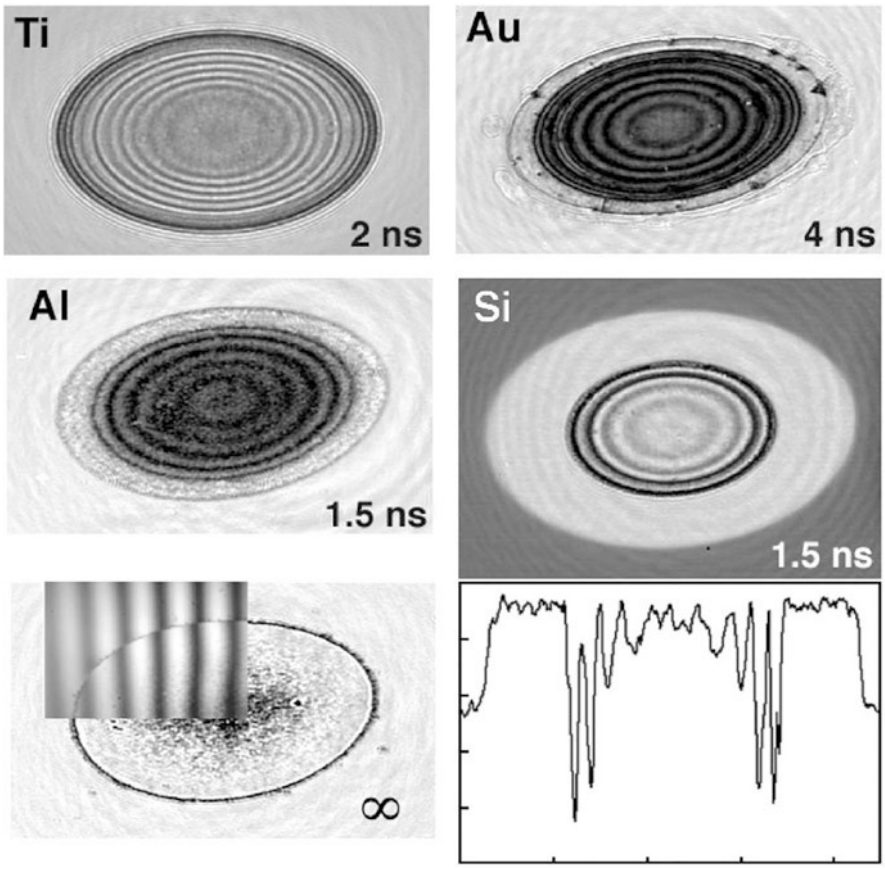

Fig. 9.3 Depth measurements through interference patterns in ultrafast imaging: top and center row: ring patterns on Ti, Au, Al, and Si with the certain delay time after the ablation. Bottom left: final surface structure of the Al film. Inset: interferogram. Bottom right: reflectivity profile for Si. (Reprinted with permission from Ref. [37])

a surface layer and initiate the ablation and then used a weak, time-delayed probe pulse to illuminate the sample surface and observed with a high-resolution optical microscope. Figure 9.3 shows the depth measurements through interference patterns in ultrafast imaging [37]. The surface profile corresponding to the transient status with different delay time can be determined by the interference ring distribution, enabling to identify the characteristic stages of the conversion of solid material into hot fluid matter undergoing ablation.

However, the strong background of specular reflections could make it difficult to discern small changes in reflection, which are often associated with nano-/microstructure formation, making it less suitable to implement in the nanostructuring field.

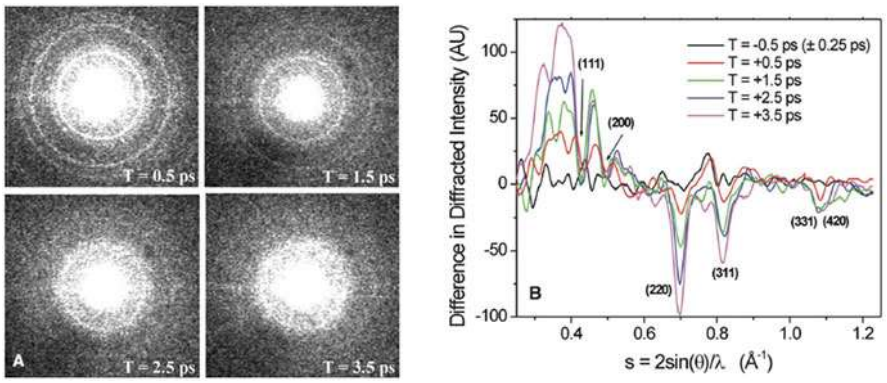

Fig. 9.4 Femtosecond electron diffraction study of an ultrafast solid-liquid phase transition in polycrystalline Al. (**a**) Sequence of diffraction patterns taken at pump-probe delay intervals (T) through the phase transition. (**b**) Radial average of the difference in diffracted intensity at different time delay. (Reprinted with permission from Ref. [43])

2.2 Ultrafast X-Ray and Electron Diffraction Imaging

Ultrafast X-ray and electron diffraction studies are more suitable for investigating long-range disorder phenomena in crystalline materials, such as melting. B. J. Siwick et al. [43] used 600-femtosecond electron pulses to study the structural evolution of aluminum (Al) during an ultrafast laser-induced solid-liquid phase transition. They observed the loss of long-range order of Al and the appearance of liquid structure by using femtosecond electron diffraction. As shown in Fig. 9.4a, the first four rings in the diffraction pattern are associated with the fcc lattice structure, which are clearly depicted at the delay time of 0.5 ps after ablation, indicating that the melting has not happened yet. At the delay time of 3.5 ps after ablation, only a single broad ring was visible, corresponding to the characteristic of liquid phase.

P. Baum et al. [45] used four-dimensional (4D) femtosecond electron diffraction method to visualize transitional structures from the initial monoclinic to the final tetragonal phase in crystalline vanadium dioxide, induced by near-infrared excitation. Three-dimensional Bragg diffraction patterns were also revealed to resolve the displacement of atoms. Figure 9.5 shows the crystal structures of vanadium dioxide phases and the Bragg diffraction patterns observed by the researchers. Figure 9.5a represents the crystal structure of monoclinic, low-temperature, and the rutile, high-temperature phase, while Fig. 9.5b shows the typical diffraction patterns observed by ultrafast electron crystallography of various crystal surfaces and zone axes.

In a more recent work, using coherent diffraction imaging with femtosecond X-ray free-electron laser (FEL), A. Barty et al. [46] captured time series snapshots of a solid evolution in ultrafast time scale with a temporal resolution of 10 ps. FEL beam is transmitted through the sample with a certain delay after the ablation caused by the visible pump laser, carrying information about the transient sample structure to

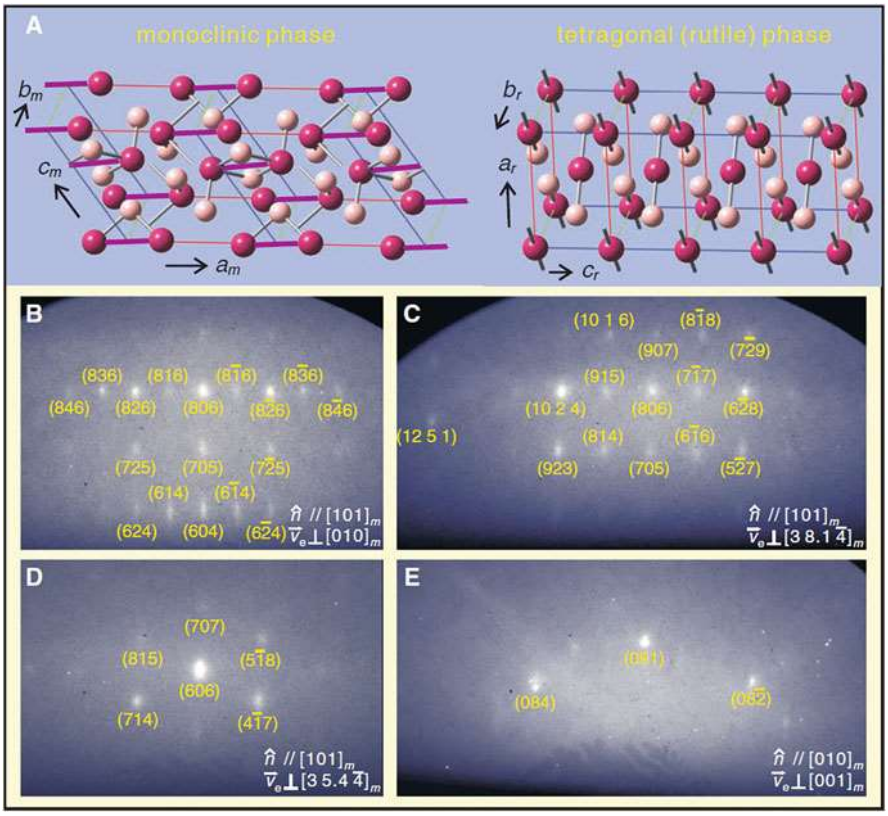

Fig. 9.5 Crystal structures of vanadium dioxide phases (**a**) and observed Bragg diffraction (**b–e**). (Reprinted with permission from Ref. [45])

the CCD detector. The real images were able to be reconstructed from the diffraction patterns at a relatively high spatial resolution due to the short wavelength of the FEL beam.

On the other hand, in some required experiments, the retrieval through diffraction images may become increasingly more difficult and less reliable at longer time delays. Diffractive imaging using time-resolved coherent XUV scattering in a transmission geometry can also be applied for indirect imaging, in which a real image was reconstructed from a diffraction pattern [44].

3 Ultrafast Pump-Probe Scatter Light Imaging

Although X-ray diffraction imaging provides a high spatial resolution of the target, it also requires extensive image reconstruction algorithms that is challenging for

delay times longer than 1 ns [46–48]. In addition, the intensity of the X-ray probe is often higher than the ablation threshold of imaged materials, making it impossible to determine the resolidification dynamics [47, 48]. For ultrafast electron diffraction imaging, although the melting process and phase transition can be inferred from the diffraction patterns [45], this technique is not a direct imaging method, and the actual form of sample cannot be visualized through this method. More recently, an ultrafast optical imaging technique was developed to investigate the structural dynamics of metals by utilizing scattered light instead of specular reflections [48–50]. Here, we will describe a scattered-light imaging technique that provides a near-zero background and high contrast, allowing to obtain high-quality real-space images of the structural dynamics of metals and resolve the complete temporal and spatial evolution of fs laser-induced morphological surface structure formation in laser-metal interactions [48–50].

3.1 Experimental Setup

The ultrafast pump-probe imaging setup is depicted in Fig. 9.6a [48–50]. An amplified Ti:sapphire laser system was used. A pump beam induced the formation of surface structures on zinc (Zn) and produced nano-/microstructures by a single laser pulse at a fluence in the range of 0.1–1.0 J cm^{-2}, under which extensive nano-/microstructure formation was observed [6].

For controlling the delay time between the pump and probe pulses, an optical delay line was used to provide various time delays, ranging from 0 to 408 ns, between the pump and probe pulses, shown in Fig. 9.6a represented by several mirrors [48–50]. A delay of 408 ns was achieved by allowing the beam to propagate over 120 m through multiple reflections. A zero delay was achieved by using the autocorrelation technique through using a BBO crystal.

After passing the delay line, the probe pulse was directed onto the BBO crystal to generate second harmonics at 400 nm. A blue band-pass filter was used to block the fundamental light after the BBO crystal and only let the 400-nm wavelength laser passing through. The 400-nm probe pulse was incident on the sample at an angle of 18°. A 50-mm (numerical aperture = 0.25) long-working-distance objective was used to image the sample surface onto the sensor of a CCD camera. The imaging optics used could resolve both nanoclusters and microstructures. More details about the measurements can be found in Ref. [49]. The formation dynamics of the transient surface structures at different delays can be tracked, and the effect of the laser fluence on their evolution can be identified, including transient surface structural fluctuations and solidification.

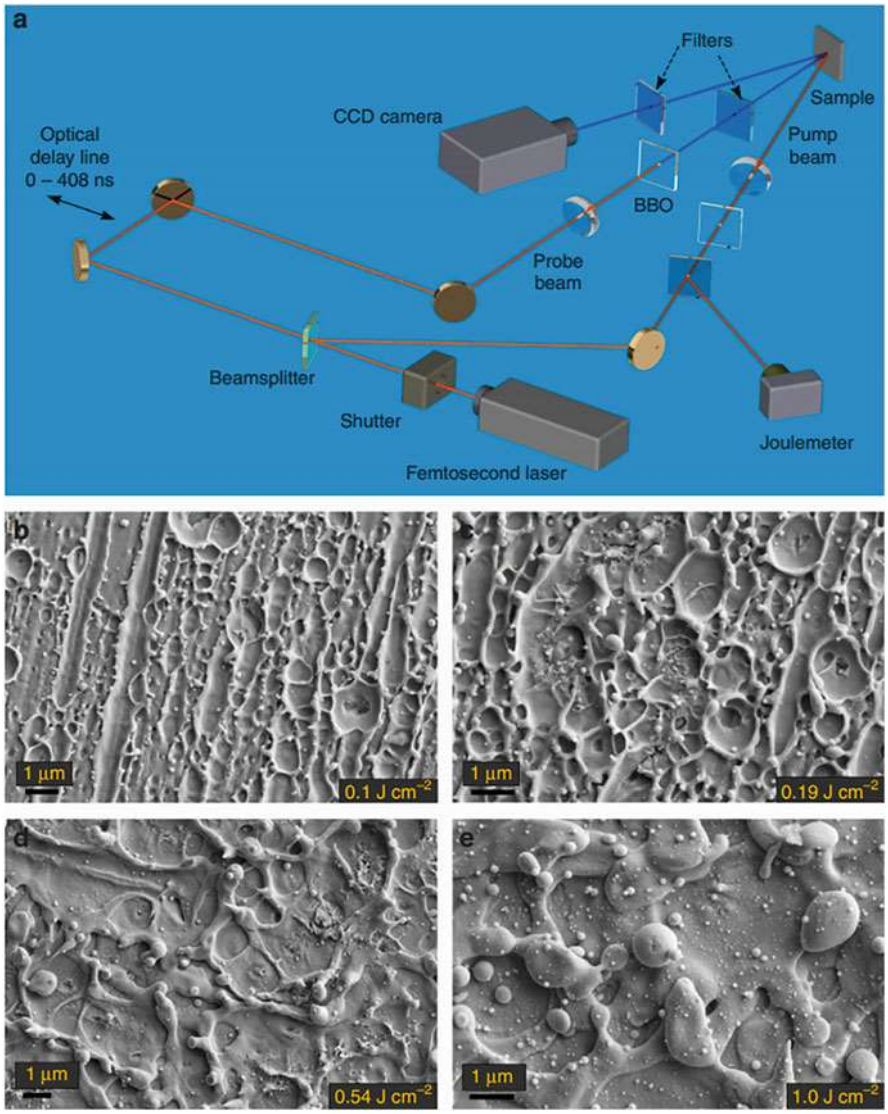

Fig. 9.6 (**a**) Ultrafast pump-probe imaging setup. (**b–e**) SEM images of surface nano-/microstructures of Zn in the center of the irradiated spot at various laser fluences, as indicated in the figure. (Reprinted with permission from Ref. [49])

3.2 Reflectance Measurements

To characterize the optical reflection variation from a surface, as the surface was irradiated with a high-intensity laser beam, and the surface reflectance at a given

fluence was crucial for the discussion, the surface reflectance was also collected at different fluences by using a hemi-ellipsoidal reflector to record both the specular and diffuse light reflection [49, 51]. Samples were placed at the internal focal point of the reflector. The reflected light was collected at the external focal point of the reflector, and its energy E_R could be measured by using a joulemeter. The reflectance $R = E_R/E_I$ was obtained from the measured E_R and E_I.

3.3 Characterization of Surface Structures

The researchers then used a scanning electron microscope (SEM) and a three-dimensional laser scanning microscope to examine the laser-induced surface nano-/microstructures after the resolidification of the surface, shown in Fig. 9.6b–e [49].

4 Nanostructuring Imaging Results and Discussions

The researchers measured the single-pulse damage threshold of the Zn sample to be 22 mJ cm^{-2}, which was determined based on the first appearance of surface modification observed under an optical microscope [49]. They also found out that nanostructures always dominate at lower fluences, while microstructures dominate at higher fluences [49], proved by Fig. 9.6b–e, which described the typical surface nano-/microstructures produced in the center of the ablated spot at various laser fluences.

To further explore the dynamics, Fig. 9.7 shows the transient structures of Zn at different delays for laser fluences of 0.1 J cm^{-2}, which are approximately four times larger than the damage threshold [49, 50]. The authors determined that the surface structures began to appear at a time delay of 400 ps, shown in Fig. 9.7c, but a comparison with the structures observed a long time after the laser pulse ($t = \infty$, from Fig. 9.7d) revealed that the two images show nearly no resemblance. The comparison indicated that the material in the irradiated spot was not yet solidified, resulting in the surface structures observed at this delay being transient. Another comparison of Fig. 9.7e, f revealed some similarity at the periphery of the irradiated spot, showing that the transient structures began to solidify at 527 ps and with increasing of delay time; the solidified area increased as well. About 90% of the surface structures were frozen at $t = 50$ ns, shown in Fig. 9.7g, h. The structures became identical to their final configuration at 124 ns, indicating that the surface structures were completely solidified at the time, shown in Fig. 9.7i, j [49].

For a fluence of 0.1 J cm^{-2}, they also found that the surface structures were dominated by extensive nanostructures with dimensions between 30 and 500 nm, and some microstructures, shown in Fig. 9.6b [49]. To fully characterized the surface structural evolution dynamics, three characteristic times were defined to evaluate the process [49, 50]:

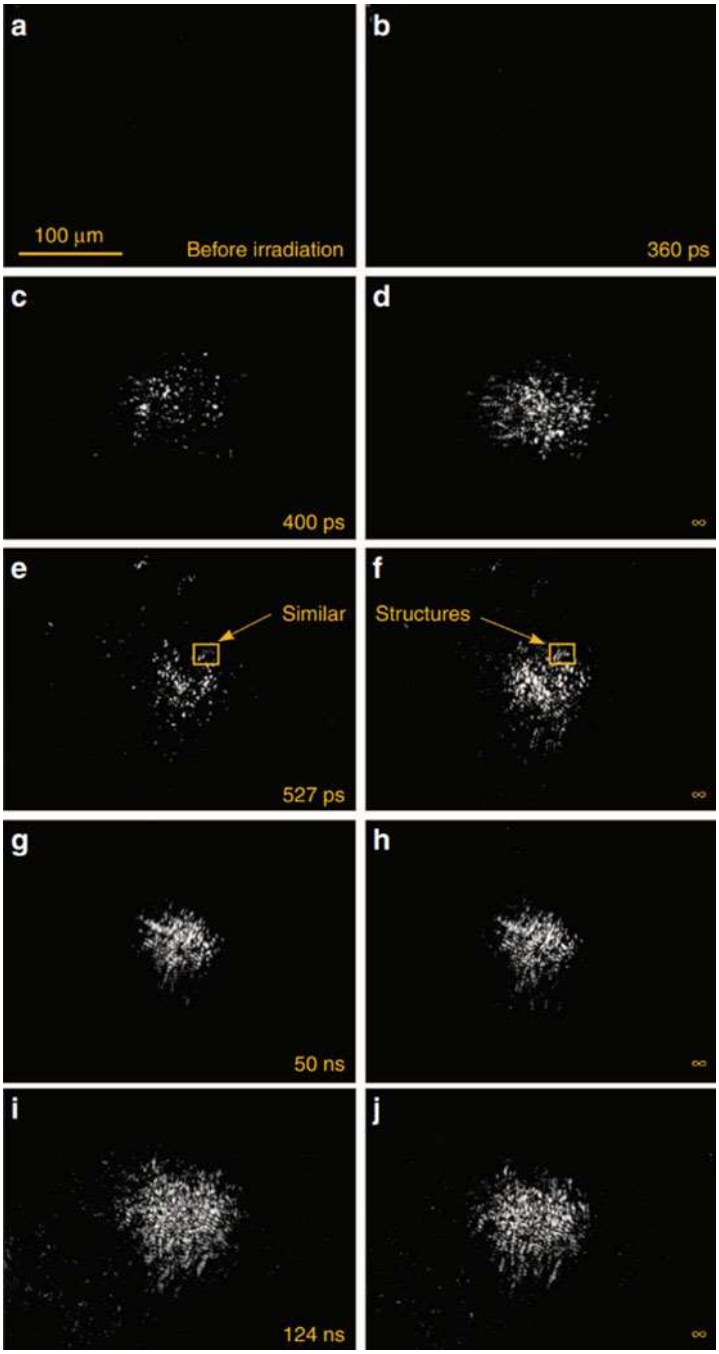

Fig. 9.7 (**a–j**) A comparison of transient surface structures observed at various delay times and final solidified structures following a pump pulse at a fluence of 0.10 J cm^{-2}. (Reprinted with permission from Ref. [49])

Table 9.1 Measurements and estimates regarding surface structural dynamics [49]

F (J cm^{-2})	t_1 (ps)	t_2 (ns)	t_3 (ns)	R	T_m (K)	t_{cool} (ns)	Ablation mechanism
0.022	–	–	–	0.57	890	–	Damage threshold
0.10	400	0.527	123.8	0.57	2970	32	Spallation
0.14	300	0.86	322	0.57	4080	41	Phase explosion
0.19	200	1.3	–	0.57	5430	50	
0.26	100	2.8	–	0.56	7320	62	
0.34	50	5	–	0.57	9480	74	
0.54	–	9.3	–	0.57	14,880	101	
0.78	–	50	–	0.55	22,330	130	
1.0	–	124	–	0.56	28,580	156	
1.1	–	–	–	0.5	–	–	Solid-density plasma regime
1.8	–	–	–	0.33	–	–	

- t_1: the time at which transient surface structures first appear
- t_2: the time at which solidification begins
- t_3: the time at which the surface structures become completely solidified

Three characteristic times were summarized for different pump fluences in Table 9.1 [49]. Fs laser-excited surface structure formation had been studied for semiconductors [36, 37], where the time required for complete solidification in silicon was found to have an upper value about 75 ns, much shorter than the analyzed data of Zn.

The mechanism of the transient surface structure formation and its associated start time, t_1, is the first to be discussed. A more previous research had shown that the characteristic time for surface melting following the ultrafast laser irradiation of Zn was about 3 ps at laser fluences of 0.1–0.15 J cm^{-2} [52]. However, the data showed that the onset of transient surface structure formation occurred at about 400 and about 300 ps at laser fluences of 0.1 and 0.14 J cm^{-2}, respectively [49].

They believed that the time difference suggested that the irradiated surface did not undergo a morphological change immediately after melting; instead, there was a time delay between the melting process and the hydrodynamic motion of the melted material that results in the transient morphological fluctuations observed on the surface. Generally, transient structural fluctuations could be induced by the flow of the melted material due to a temperature gradient (the Marangoni effect) and the flow due to laser-induced stresses in the melted surface layer. To identify whether the Marangoni effect plays the key role, they estimated the characteristic timescale t_M of the Marangoni effect through the formula [53]:

$$t_{\mathrm{M}} = \frac{\eta L^2}{|\gamma_T|\, T_{\mathrm{m}} h} \tag{9.1}$$

where η is the dynamic viscosity of the melt, L is the typical radial dimension, h is the average melt depth, T_{m} is the melting point of the metal, and $|\gamma_T| = |d\gamma/dT|$ represents the absolute value of the temperature coefficient of the surface tension γ. By using the values of $\eta = 2.5 \times 10^{-3}$ Pa s [54], $|\gamma_T| = 0.25 \times 10^{-3}$ N m^{-1} K^{-1} [55], $T_{\mathrm{m}} = 693$ K, and $L = 200$ nm and assumed $h = 30$ nm, they got $t_{\mathrm{M}} \approx 20$ ns to be the obtained result, which is two orders of magnitude larger than the observed values of t_1 [49]. Therefore, they proved that the Marangoni effect did not appear to be the primary cause of the onset of the transient surface structures. However, this did not exclude the Marangoni effect as a factor affecting the formation of surface structures at longer timescales.

Following high-intensity ultrashort laser pulse heating and as a result of isochoric heating, a highly pressurized melted surface layer can be formed, which also had been theoretically predicted in more previous work [56, 57]. Pressure relaxation in this melted layer will induce hydrodynamic motion, resulting in morphological fluctuations on the surface. The timescale of those morphological fluctuations is governed by the speed of sound in the melted material [57] and can be estimated as $t_{\mathrm{P}} \approx L/v_{\mathrm{sl}}$, where v_{sl} represents the speed of sound in liquid Zn, as the value is 3.8×10^3 m s^{-1} [58] in solid Zn, and the speed of in liquid metals is 1.5 times smaller than that in solids. Therefore, assuming $v_{\mathrm{sl}} = 2.3 \times 10^3$ m s^{-1} and again using the typical radial dimension $L = 200$ nm found from Fig. 9.6b, $t_{\mathrm{P}} \approx 90$ ps was obtained, which is on the same timescale as the measured t_1 values [49].

In general, melting occurs at laser fluences near the damage threshold, and ablation occurs at higher fluences. The laser fluence was more than four times greater than the damage threshold [49]. The start time of transient surface structure formation, t_1, was associated with ablation driven by pressure relaxation in the surface layer, as determined by the Fig. 9.8, whereas Fig. 9.8 presents t_1 and t_2 as functions of the laser fluence. Also from the figure, t_1 decreases with laser fluence, which indicates an earlier onset of ablation due to higher pressure in the surface layer [49].

Figure 9.9 shows a series of time-resolved surface images acquired at various delays following pump pulse irradiation at a higher fluence of 0.78 and 1.0 J cm^{-2} separately [49, 50]. Counterintuitively, it can be seen that transient surface structures first appeared at the edge of the irradiated spot and formed a ring, in contrast to what occurred under ablation at lower laser fluences, for which the transient structures first appear in the center (from Fig. 9.7c) [49, 50]. Over time, the transient surface structures moved toward the center. At 5–9.3 ns, the center of the irradiated spot was covered with structures. The solidification of the transient surface structures began at about 124 ns, as indicated by the resemblance to the final image. At the longest delay investigated in the experiments (408 ns), they found out that the solidification was not fully completed, as a difference was still existing between Fig. 9.9k, l. Then

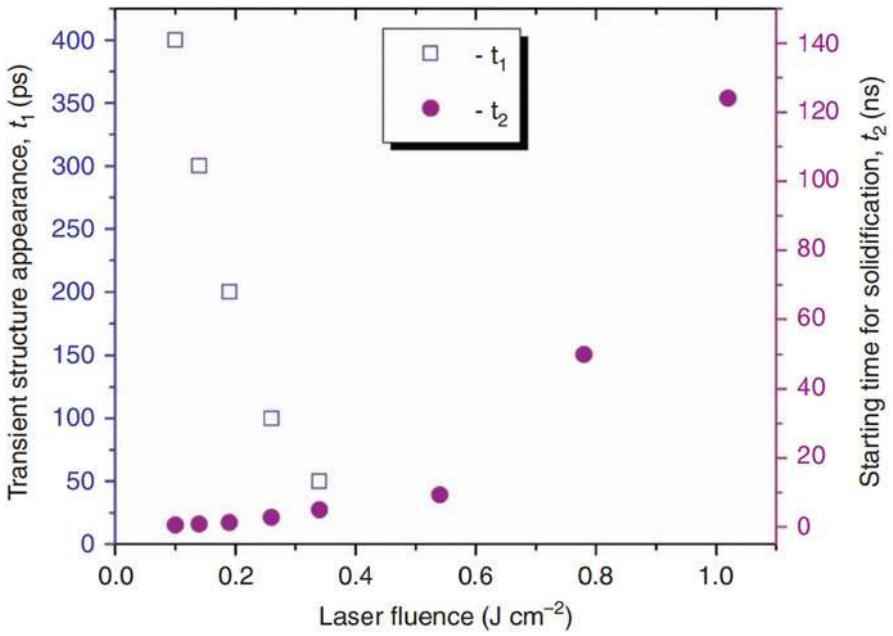

Fig. 9.8 Time at which transient surface structures appear, t_1, and start time of solidification, t_2, as functions of laser fluence. (Reprinted with permission from Ref. [49])

they made a comparison of Figs. 9.7 and 9.9 and showed that the spatial sequencing of the transient structures before solidification varied with the laser fluence. To further understand this dependence, the authors considered the surface images to be acquired at a fixed delay time of 527 ps, but at different laser fluences, as shown in Fig. 9.10, a transition can be seen from first emergence of the transient structures in the center to first emergence at the edge that occurs at 0.54 J cm^{-2}. the SEM images presented in Fig. 9.6 to show that at this laser fluence, the surface structures in the center changed from being mostly nanostructures to being mostly microstructures, corresponding to the CCD images [49].

At these higher laser fluences, nanostructures could be produced at the edge of the ablated spot because of the Gaussian profile of the laser beam. Therefore, the spatial evolution of the ring surface pattern observed between 300 ps and 2.8 ns in Fig. 9.9 is attributed to the fact that nanostructures first form at the surrounding area, and the center region is later populated with microstructures; with regard to the timescale of morphological fluctuations ($t_P \approx L/v_{sl}$), the time required to form nanostructures (corresponding to smaller L) was shorter than that required to form microstructures (corresponding to larger L) [49]. Another possible explanation for the central dark spot is that the formation of highly light-absorptive matter in the central part of the interaction area was possibly due to the formation of an ablation plasma that masks the surface structures. Over time, such an ablation plasma would become more transparent, and the surface structures in the central part of the ablated

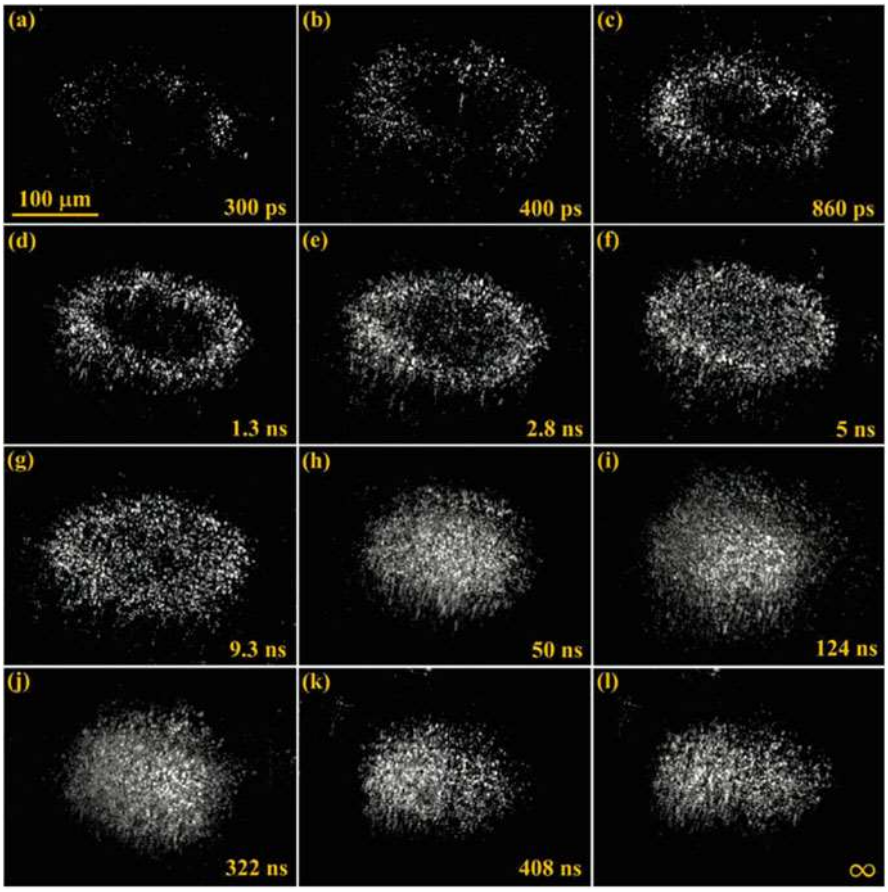

Fig. 9.9 (**a–l**) CCD images of a Zn surface at various delay times following a pump pulse at a fluence of 0.78 J cm^{-2}. (Reprinted with permission from Ref. [49])

area would become more visible [49, 50]. The absorption of laser light by an ablation plasma has been previously observed in more previous research of double-pulse ablation studies [59, 60].

Several possible ablation mechanisms exist [56, 57, 61–63] to describe the mechanisms of the evolution of the transient surface structures from their first appearance (t_1) up through the onset of solidification (t_2), including evaporation [62], thermomechanical fragmentation/spallation [56, 57], and phase explosion [56, 63]. The maximum lattice temperature T_m should also be estimated to identify the ablation mechanisms that were responsible to the former observations [52, 64]:

$$T_\mathrm{m} = T_0 + \frac{F_\mathrm{A}}{c_i}\frac{\beta\alpha}{\beta+\alpha}, \beta = \sqrt{\frac{g}{\kappa}} \tag{9.2}$$

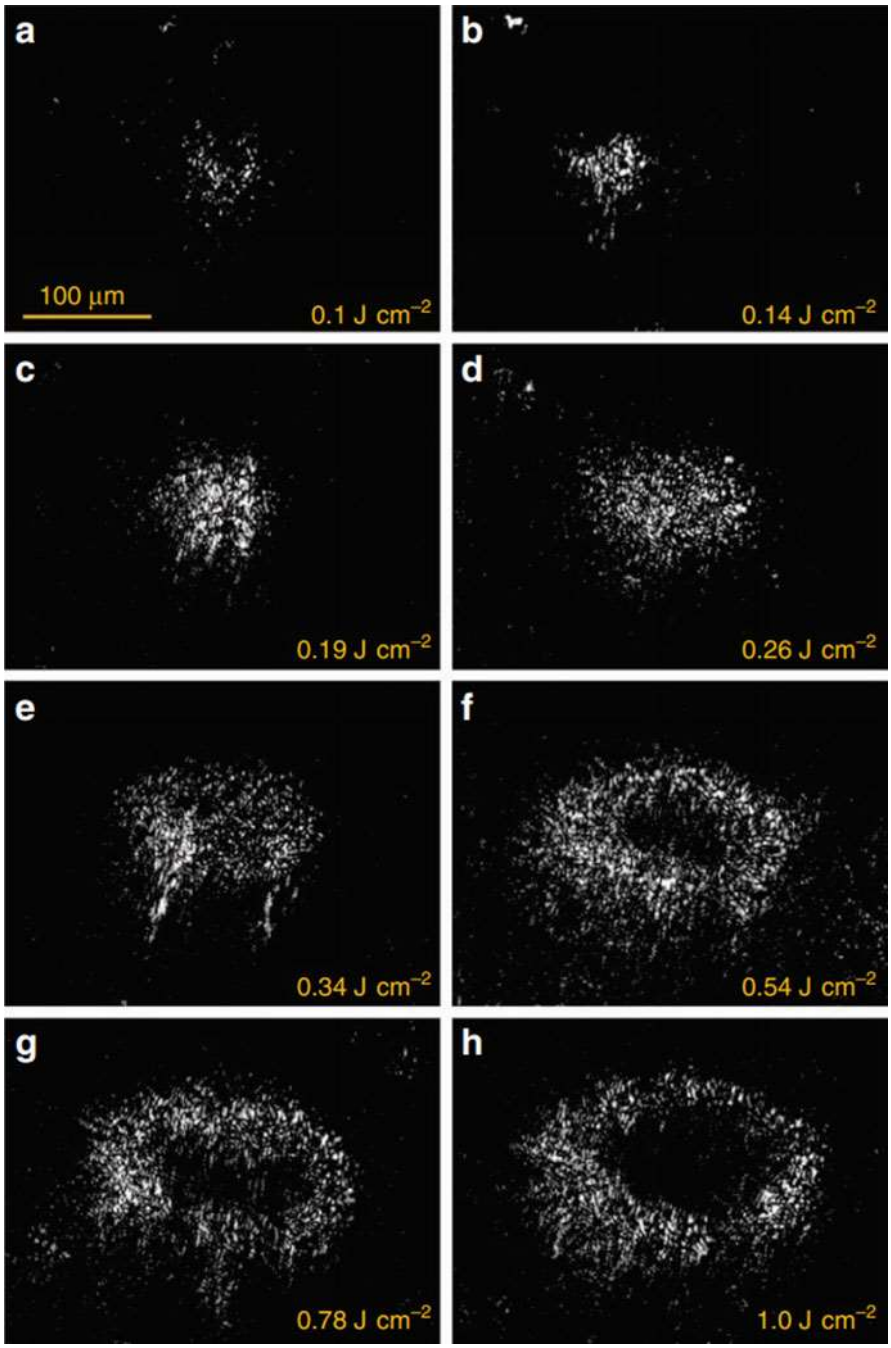

Fig. 9.10 (**a–h**) CCD images of Zn surfaces at a fixed delay time of 527 ps following pump pulses at various laser fluence values. (Reprinted with permission from Ref. [49])

where T_0 is the room temperature, c_i is the specific heat of the lattice, α is the light attenuation coefficient, g is the electron-phonon coupling factor, κ is the thermal conductivity, and $\phi_A = (1 - R)\phi$ is the absorbed laser fluence [51], where R is the reflectance of Zn at the wavelength of the laser used. The reflectance of a metal surface depends on its condition after polishing, the angle of the incident light, and the laser fluence. The key to obtaining a reliable estimate of the surface temperature was to accurately determine the value of the sample reflectance under the experimental conditions. To do so, they performed a rigorous surface reflectance measurement by using a hemi-ellipsoidal collector to collect both the specular and diffuse reflected light [49, 51]. The measured reflectance in a fluence range of 0.01–1.0 J cm^{-2} was $R = 0.55$–0.57, shown in Table 9.1 [49]. Table 9.1 also shows the surface temperatures estimated by using $T_0 = 300$ K, $c_i = 2.78 \times 106$ J m^{-3} K^{-1}, $\alpha = 7.5 \times 10^7$ m^{-1}, $g = 6 \times 10^{16}$ W m^{-3} K^{-1} [65], and $\kappa = 116$ W m^{-1} K^{-1} [49]. At the damage threshold laser fluence of 0.022 J cm^{-2}, T_m was estimated to be 890 K, only slightly higher than the melting point of Zn (693 K), indicating that (Eq. 9.2) provided a reasonable estimation of the surface temperature.

At $\phi = 0.1$ J cm^{-2}, the surface temperature was estimated to be 2970 K, exceeding the boiling point of Zn (1180 K), and this laser fluence was in the ablation regime [49]. At laser fluences of 0.14 J cm^{-2} or above, the estimated surface temperatures are above the thermodynamic critical point T_c (3190 K), indicating that the laser-excited material becomes a supercritical fluid (with no distinction between the liquid and vapor phases). The authors discussed that the surface temperature for ablation at $F = 0.1$ J cm^{-2} could lead to either vaporization [62] or thermomechanical fragmentation/spallation [49, 56, 57]. However, it is believed that the predominant contribution to ablation was from thermomechanical fragmentation/spallation, whereas the role of vaporization was not essential [66]. Therefore, it is believed that the results at a fluence of 0.1 J cm^{-2} were mostly related to ablation through the spallation mechanism. In the spallation regime, an ultrashort laser pulse induces fast isochoric heating of the surface layer [56, 57, 67–69], which causes a buildup of high stress, cavitation, nanofoam formation, and thermomechanical spallation (ablation) of a liquid layer on the surface due to the relaxation of tensile stresses developed in the surface layer.

In a more recent follow-up work, the same research lab used a similar ultrafast imaging technique to record the spatiotemporal evolution of the nanostructures induced by femtosecond laser ablation [48]. The evolution underwent melting, spallation, and resolidification process. Finite-difference time-domain (FDTD) simulation was also performed and showed consistency with molecular dynamics simulations, showing that the photomechanical spallation was leading the melting of nanostructure for a few picoseconds. Figure 9.11 shows the difference of FDTD calculation of scattering through liquid and solid Zn sphere and schematics of photomechanical spallation process in surface nanostructures which was done in the work [48].

For an incident laser fluence of higher than 0.14 J cm^{-2}, the surface temperature is estimated to be significantly higher than 0.9 T_c [49], which is the characteristic threshold temperature for phase explosion [63]. Phase explosion occurs at laser

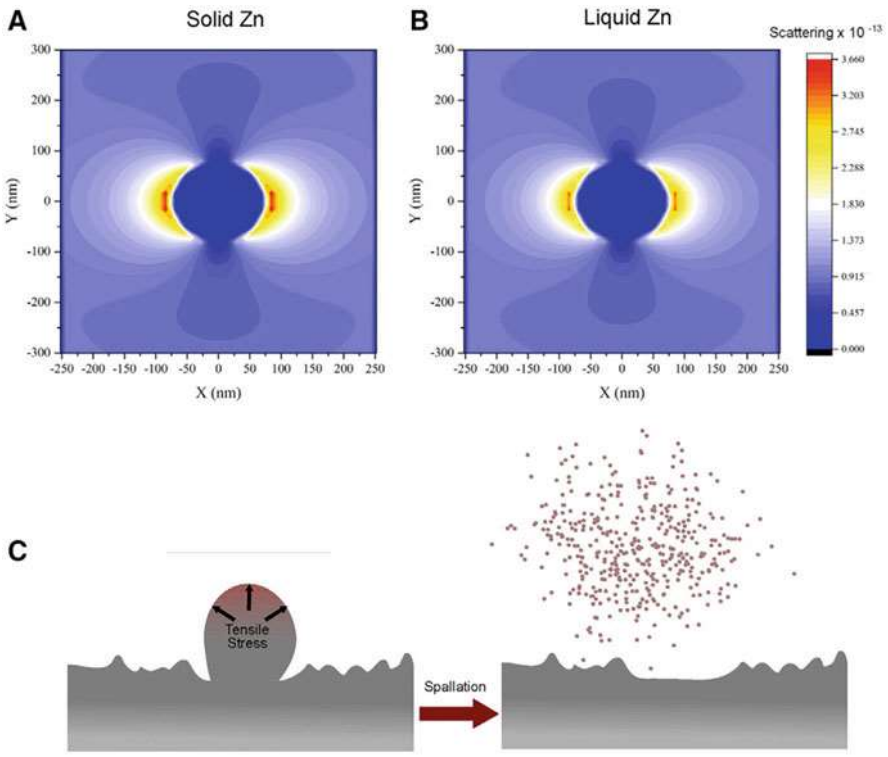

Fig. 9.11 (**a**, **b**) FDTD calculation of scattering from a 150 nm (**a**) solid Zn sphere and (**b**) liquid Zn sphere. (**c**) Schematics of photomechanical spallation process in surface nanostructures. (Reprinted with permission from Ref. [48])

fluences below those for substantial ionization and plasma formation [69]. It is known that plasma formation causes a significant decrease in reflectance [49, 51, 70]. The reflectance measurements recorded in Table 9.1 shows that a significant decrease in the reflectance of the Zn surface occurs at laser fluences above 1.1 J cm^{-2}. The result indicates that in the laser fluence range of 0.14–1.1 J cm^{-2}, ablation is primarily caused by phase explosion. Therefore, the authors inferred that the transient structural dynamics between t_1 and t_2 originate from either the spallation mechanism or the phase explosion mechanism, depending on the laser fluence [49]. As shown in Fig. 9.8, both t_1 and t_2 depend on the laser fluence. The start time of solidification, t_2, increases with laser fluence, indicating that a longer time is required for solidification to occur at a higher laser fluence [49].

The discussion of mechanism of complete solidification and its associated time, t_3, was also put forward [49]. After ablation, rapid cooling due to high electronic heat conduction causes solidification of the melted surface layer, giving rise to permanent surface structures. The cooling and resolidification of the melted surface layer in the spallation regime had been previously modeled by using the atomistic

molecular dynamics method combined with a continuum-level two-temperature model by other researchers [67, 68]. In those more previous works, the complete resolidification time was predicted to be 2.5 ns for Al [67] and 1.4–1.7 ns for Ag [68]. Those timescales were approximately two orders of magnitude smaller than the observed complete solidification time, t_3, for Zn. It is generally believed that the cooling of an ultrafast laser-heated metal surface is dominated by thermal conduction [52, 64]. Under these conditions, the cooling time t_{cool} is estimated to be [52]

$$t_{\text{cool}} = \frac{\delta^2}{4\chi}, \delta = \left(\frac{18 I_{\text{A}} k}{g^2 T_0}\right)^{\frac{1}{3}} \tag{9.3}$$

where χ is the thermal diffusivity and I_{A} is the absorbed laser intensity. The estimated values of t_{cool} for Zn are also shown in Table 9.1, where it can be seen that t_{cool} is significantly shorter than t_3 from observation. Following this way, both the model predictions [67, 68] and the estimation based on the equation predicted significantly faster cooling than the observation in the experiments, indicating that the current understanding of the rapid cooling process was incomplete [49]. To explain this discrepancy, it was suggested that the slower cooling process was due to an enhanced thermal coupling [49], which had previously been observed and modeled [71, 72], where it was found that a significant amount of thermal energy remains in a metal following fs laser ablation, as the transfer time of thermal energy from the ablation plume back to the sample is much longer than the laser pulse duration in the time domain. The speculation was supported by other researchers of residual thermal coupling in the ablation of Zn [71], which indicated that the starting point of the enhanced thermal coupling occurs at $\phi = 0.45$ J cm^{-2} and is correlated with an abrupt increase in the start time of solidification, t_2, where $\phi >$ 0.54 J cm^{-2}, shown in Fig. 9.8 [49]. Moreover, the heating of a sample through the transfer of energy from the ablation plasma was found to cause ultradeep drilling of the material in more previous research [73]. In addition to the enhanced thermal coupling, surface cooling can also be slowed by the latent heat of resolidification and by exothermic chemical reactions induced during laser ablation [74]. In one example of the large contribution of chemical sources of energy, this contribution has been shown to reach up to 30% of the incident laser energy during the nanosecond laser ablation of Zn in air [74].

5 Summary and Outlook

In conclusion, by using the ultrafast pump-probe imaging technique, the researchers have captured and visualized the complete temporal and spatial evolution of the fs laser-induced surface structural dynamics of metals. The transient surface structures were found by the researchers to first appear at a delay time on the order of 100 ps,

and this is attributed to ablation driven by pressure relaxation in the surface layer. At lower laser fluences that favor nanostructure formation, the transient surface structures first appear in the central portion of the ablated spot. At higher laser fluences that favor microstructure formation, nanostructures first emerge at the periphery, and the center region is later populated with microstructures [49].

The visualization and control of surface structural dynamics not only are of fundamental importance for understanding the fs laser-induced responses of materials but also pave the way for the design of new material functionalities through surface structuring.

References

1. A.Y. Vorobyev, C. Guo, Direct femtosecond laser surface nano/microstructuring and its applications. Laser Photonics Rev. **7**, 385–407 (2013)
2. Y. He, J. Zhang, S. Singh, E. Garcell, A.Y. Vorobyev, B. Lam, Z. Zhan, J. Yang, C. Guo, Maskless laser nano-lithography of glass through sequential activation of multi-threshold ablation. Appl. Phys. Lett. **114**, 133107 (2019)
3. J. Zhang, C. Cong, C. Guo, Single-step maskless nano-lithography on glass by femtosecond laser processing. J. Appl. Phys. **127**, 163102 (2020)
4. P. Pronko, S. Dutta, J. Squier, J. Rudd, D. Du, G. Mourou, Machining of sub-micron holes using a femtosecond laser at 800 nm. Opt. Commun. **114**, 106–110 (1995)
5. F. Korte, J. Serbin, J. Koch, A. Egbert, C. Fallnich, A. Ostendorf, B. Chichkov, Towards nanostructuring with femtosecond laser pulses. Appl. Phys. A **77**, 229–235 (2003)
6. A.Y. Vorobyev, C. Guo, Femtosecond laser nanostructuring of metals. Opt. Express **14**, 2164–2169 (2006)
7. A. Vorobyev, C. Guo, Multifunctional surfaces produced by femtosecond laser pulses. J. Appl. Phys. **117**, 033103 (2015)
8. S. Nolte, B. Chichkov, H. Welling, Y. Shani, K. Lieberman, H. Terkel, Nanostructuring with spatially localized femtosecond laser pulses. Opt. Lett. **24**, 914–916 (1999)
9. C. Wu, C. Crouch, L. Zhao, J. Carey, R. Younkin, J. Levinson, E. Mazur, R. Farrell, P. Gothoskar, A. Karger, Near-unity below-band-gap absorption by microstructured silicon. Appl. Phys. Lett. **78**, 1850–1852 (2001)
10. A. Pereira, A. Cros, P. Delaporte, S. Georgiou, A. Manousaki, W. Marine, M. Sentis, Surface nanostructuring of metals by laser irradiation: Effects of pulse duration, wavelength and gas atmosphere. Appl. Phys. A **79**, 1433–1437 (2004)
11. A. Borowiec, H.K. Haugen, Subwavelength ripple formation on the surfaces of compound semiconductors irradiated with femtosecond laser pulses. Appl. Phys. Lett. **82**, 4462–4464 (2003)
12. J. Bonse, M. Munz, H. Sturm, Structure formation on the surface of indium phosphide irradiated by femtosecond laser pulses. J. Appl. Phys. **97**, 013538 (2005)
13. F. Costache, S. Kouteva-Arguirova, J. Reif, Sub–damage–threshold femtosecond laser ablation from crystalline Si: Surface nanostructures and phase transformation. Appl. Phys. A **79**, 1429–1432 (2004)
14. A. Vorobyev, C. Guo, Direct creation of black silicon using femtosecond laser pulses. Appl. Surf. Sci. **257**, 7291–7294 (2011)
15. A. Kabashin, M. Charbonneau-Lefort, M. Meunier, R. Leonelli, Effects of deposition and post-fabrication conditions on photoluminescent properties of nanostructured Si/SiOx films prepared by laser ablation. Appl. Surf. Sci. **168**, 328–331 (2000)

16. A. Vorobyev, C. Guo, Enhanced absorptance of gold following multipulse femtosecond laser ablation. Phys. Rev. B **72**, 195422 (2005)
17. Y.P. Meshcheryakov, N. Bulgakova, Thermoelastic modeling of microbump and nanojet formation on nanosize gold films under femtosecond laser irradiation. Appl. Phys. A **82**, 363–368 (2006)
18. D.S. Ivanov, B. Rethfeld, G.M. O'Connor, T.J. Glynn, A.N. Volkov, L.V. Zhigilei, The mechanism of nanobump formation in femtosecond pulse laser nanostructuring of thin metal films. Appl. Phys. A **92**, 791–796 (2008)
19. A.Y. Vorobyev, C. Guo, Colorizing metals with femtosecond laser pulses. Appl. Phys. Lett. **92**, 041914 (2008)
20. A.Y. Vorobyev, C. Guo, Femtosecond laser blackening of platinum. J. Appl. Phys. **104**, 053516 (2008)
21. A.Y. Vorobyev, C. Guo, Antireflection effect of femtosecond laser-induced periodic surface structures on silicon. Opt. Express **19**, A1031–A1036 (2011)
22. T. Baldacchini, J.E. Carey, M. Zhou, E. Mazur, Superhydrophobic surfaces prepared by microstructuring of silicon using a femtosecond laser. Langmuir **22**, 4917–4919 (2006)
23. M. Barberoglou, V. Zorba, E. Stratakis, E. Spanakis, P. Tzanetakis, S.H. Anastasiadis, C. Fotakis, Bio-inspired water repellent surfaces produced by ultrafast laser structuring of silicon. Appl. Surf. Sci. **255**, 5425–5429 (2009)
24. E. Fadeeva, S. Schlie, J. Koch, B.N. Chichkov, A.Y. Vorobyev, C. Guo, *Contact Angle, Wettability and Adhesion*, vol 6 (VSP/Brill, 2009)
25. A. Vorobyev, C. Guo, Water sprints uphill on glass. J. Appl. Phys. **108**, 123512 (2010)
26. S.C. Singh, M. ElKabbash, Z. Li, X. Li, B. Regmi, M. Madsen, S.A. Jalil, Z. Zhan, J. Zhang, C. Guo, Solar-trackable super-wicking black metal panel for photothermal water sanitation. Nat. Sustain. **3**, 938–946 (2020)
27. A.Y. Vorobyev, C. Guo, Laser turns silicon superwicking. Opt. Express **18**, 6455–6460 (2010)
28. R.V. Volkov, D.M. Golishnikov, V.M. Gordienko, A.B. Savel'ev, Overheated plasma at the surface of a target with a periodic structure induced by femtosecond laser radiation. J. Exp. Theor. Phys. Lett. **77**, 473–476 (2003)
29. T.Y. Hwang, A.Y. Vorobyev, C. Guo, Surface-plasmon-enhanced photoelectron emission from nanostructure-covered periodic grooves on metals. Phys. Rev. B **79**, 085425 (2009)
30. A.Y. Vorobyev, V.S. Makin, C. Guo, Brighter light sources from black metal: Significant increase in emission efficiency of incandescent light sources. Phys. Rev. Lett. **102**, 234301 (2009)
31. S.A. Jalil, M. Akram, J.A. Bhat, J.J. Hayes, S.C. Singh, M. ElKabbash, C. Guo, Creating superhydrophobic and antibacterial surfaces on gold by femtosecond laser pulses. Appl. Surf. Sci. **506**, 144952 (2020)
32. E. Fadeeva, V.K. Truong, M. Stiesch, B.N. Chichkov, R.J. Crawford, J. Wang, E.P. Ivanova, Bacterial retention on superhydrophobic titanium surfaces fabricated by femtosecond laser ablation. Langmuir **27**, 3012–3019 (2011)
33. A. Cunha, A.-M. Elie, L. Plawinski, A.P. Serro, A.M.B. do Rego, A. Almeida, M.C. Urdaci, M.-C. Durrieu, R. Vilar, Femtosecond laser surface texturing of titanium as a method to reduce the adhesion of Staphylococcus aureus and biofilm formation. Appl. Surf. Sci. **360**, 485–493 (2016)
34. M. Downer, R.L. Fork, C.V. Shank, Femtosecond imaging of melting and evaporation at a photoexcited silicon surface. J. Opt. Soc. Am. B **2**, 595–599 (1985)
35. J. Bonse, G. Bachelier, J. Siegel, J. Solis, H. Sturm, Time-and space-resolved dynamics of ablation and optical breakdown induced by femtosecond laser pulses in indium phosphide. J. Appl. Phys. **103**, 054910 (2008)
36. D. Von der Linde, K. Sokolowski-Tinten, The physical mechanisms of short-pulse laser ablation. Appl. Surf. Sci. **154**, 1–10 (2000)
37. K. Sokolowski-Tinten, J. Bialkowski, A. Cavalleri, D. von der Linde, A. Oparin, J. Meyer-ter-Vehn, S. Anisimov, Transient states of matter during short pulse laser ablation. Phys. Rev. Lett. **81**, 224 (1998)

38. J. Bonse, G. Bachelier, J. Siegel, J. Solis, Time-and space-resolved dynamics of melting, ablation, and solidification phenomena induced by femtosecond laser pulses in germanium. Phys. Rev. B **74**, 134106 (2006)
39. M. Domke, S. Rapp, M. Schmidt, H.P. Huber, Ultrafast pump-probe microscopy with high temporal dynamic range. Opt. Express **20**, 10330–10338 (2012)
40. J. Hernandez-Rueda, D. Puerto, J. Siegel, M. Galvan-Sosa, J. Solis, Plasma dynamics and structural modifications induced by femtosecond laser pulses in quartz. Appl. Surf. Sci. **258**, 9389–9393 (2012)
41. C.W. Siders, A. Cavalleri, K. Sokolowski-Tinten, C. Tóth, T. Guo, M. Kammler, M.H. Von Hoegen, K.R. Wilson, D. von der Linde, C.P. Barty, Detection of nonthermal melting by ultrafast X-ray diffraction. Science **286**, 1340–1342 (1999)
42. A. Rousse, C. Rischel, S. Fourmaux, I. Uschmann, S. Sebban, G. Grillon, P. Balcou, E. Förster, J.-P. Geindre, P. Audebert, Non-thermal melting in semiconductors measured at femtosecond resolution. Nature **410**, 65–68 (2001)
43. B.J. Siwick, J.R. Dwyer, R.E. Jordan, R.J.D. Miller, An atomic-level view of melting using femtosecond electron diffraction. Science **302**, 1382–1385 (2003)
44. K. Sokolowski-Tinten, A. Barty, S. Boutet, U. Shymanovich, H. Chapman, M. Bogan, S. Marchesini, S. Hau-Riege, N. Stojanovic, J. Bonse, Y. Rosandi, H.M. Urbassek, R.A. Tobey, H. Ehrke, A. Cavalleri, S. Düsterer, H. Redlin, M. Frank, S. Bajt, J. Schulz, M. Seibert, J. Hajdu, R. Treusch, C. Bostedt, M. Hoener, T. Möller, Short-pulse laser induced transient structure formation and ablation studied with time-resolved coherent XUV-scattering. MRS Online Proc. Libr. **1230**, 1–6 (2009)
45. P. Baum, D.-S. Yang, A.H. Zewail, 4D visualization of transitional structures in phase transformations by electron diffraction. Science **318**, 788–792 (2007)
46. A. Barty, S. Boutet, M.J. Bogan, S. Hau-Riege, S. Marchesini, K. Sokolowski-Tinten, N. Stojanovic, H. Ehrke, A. Cavalleri, S. Düsterer, Ultrafast single-shot diffraction imaging of nanoscale dynamics. Nat. Photonics **2**, 415–419 (2008)
47. J. Spence, Ultrafast diffract-and-destroy movies. Nat. Photonics **2**, 390–391 (2008)
48. M. ElKabbash, R. Fang, A. Vorobyev, S.A. Jalil, S. Chamoli, B. Lam, S. Singh, C. Guo, Imaging nanostructure phase transition through ultrafast far-field optical ultra-microscopy. Cell Rep. Phys. Sci. **2**, 100651 (2021)
49. R. Fang, A. Vorobyev, C. Guo, Direct visualization of the complete evolution of femtosecond laser-induced surface structural dynamics of metals. Light Sci. Appl. **6**, e16256–e16256 (2017)
50. R. Fang, A.Y. Vorobyev, S.C. Singh, C. Guo, Ultrafast microscopy in resolving femtosecond laser-induced surface structuring. Jpn. J. Appl. Phys. **57**, 08PF04 (2018)
51. A. Vorobyev, C. Guo, Reflection of femtosecond laser light in multipulse ablation of metals. J. Appl. Phys. **110**, 043102 (2011)
52. M. Agranat, S. Ashitkov, V. Fortov, A. Kirillin, A. Kostanovskii, S. Anisimov, P. Kondratenko, Use of optical anisotropy for study of ultrafast phase transformations at solid surfaces. Appl. Phys. A **69**, 637–640 (1999)
53. J. Bonse, S. Wiggins, J. Solis, Phase transitions induced by femtosecond laser pulse irradiation of indium phosphide. Appl. Surf. Sci. **248**, 151–156 (2005)
54. M.J. Assael, I.J. Armyra, J. Brillo, S.V. Stankus, J. Wu, W.A. Wakeham, Reference data for the density and viscosity of liquid cadmium, cobalt, gallium, indium, mercury, silicon, thallium, and zinc. J. Phys. Chem. Ref. Data **41**, 033101 (2012)
55. K. Nogi, K. Ogino, A. McLean, W. Miller, The temperature coefficient of the surface tension of pure liquid metals. Metall. Trans. B **17**, 163–170 (1986)
56. E. Leveugle, D.S. Ivanov, L.V. Zhigilei, Photomechanical spallation of molecular and metal targets: Molecular dynamics study. Appl. Phys. A **79**, 1643–1655 (2004)
57. N. Inogamov, A.Y. Faenov, V. Zhakhovskii, I.Y. Skobelev, V. Khokhlov, Y. Kato, M. Tanaka, T. Pikuz, M. Kishimoto, M. Ishino, Interaction of short laser pulses in wavelength range from infrared to X-ray with metals, semiconductors, and dielectrics. Contrib. Plasma Physics **51**, 361–366 (2011)
58. D.R. Lide, *CRC Handbook of Chemistry and Physics*, vol 85 (CRC Press, 2004)

59. A. Semerok, C. Dutouquet, Ultrashort double pulse laser ablation of metals. Thin Solid Films **453**, 501–505 (2004)
60. M. Povarnitsyn, T. Itina, K. Khishchenko, P. Levashov, Suppression of ablation in femtosecond double-pulse experiments. Phys. Rev. Lett. **103**, 195002 (2009)
61. N.M. Bulgakova, R. Stoian, A. Rosenfeld, I.V. Hertel, *Laser-Surface Interactions for New Materials Production* (Springer, 2010), pp. 81–97
62. S.I. Anisimov, B. Luk'Yanchuk, Selected problems of laser ablation theory. Physics-Uspekhi **45**, 293 (2002)
63. A. Miotello, R. Kelly, Critical assessment of thermal models for laser sputtering at high fluences. Appl. Phys. Lett. **67**, 3535–3537 (1995)
64. S.I. Anisimov, B. Rethfeld, *Nonresonant Laser-Matter Interaction (NLMI-9)* (International Society for Optics and Photonics, 1997), pp. 192–203
65. M.V. Shugaev, N.M. Bulgakova, Thermodynamic and stress analysis of laser-induced forward transfer of metals. Appl. Phys. A **101**, 103–109 (2010)
66. N. Inogamov, V. Zhakhovskii, V. Khokhlov, Jet formation in spallation of metal film from substrate under action of femtosecond laser pulse. J. Exp. Theor. Phys. **120**, 15–48 (2015)
67. N.A. Inogamov, V.V. Zhakhovsky, V.A. Khokhlov, S.I. Ashitkov, Y.N. Emirov, K.V. Khichshenko, A.Y. Faenov, T.A. Pikuz, M. Ishino, M. Kando, *Journal of Physics: Conference Series* (IOP Publishing, 2014), p. 012041
68. C. Wu, M.S. Christensen, J.-M. Savolainen, P. Balling, L.V. Zhigilei, Generation of subsurface voids and a nanocrystalline surface layer in femtosecond laser irradiation of a single-crystal Ag target. Phys. Rev. B **91**, 035413 (2015)
69. L.V. Zhigilei, Z. Lin, D.S. Ivanov, Atomistic modeling of short pulse laser ablation of metals: Connections between melting, spallation, and phase explosion. J. Phys. Chem. C **113**, 11892–11906 (2009)
70. S. Kirkwood, Y. Tsui, R. Fedosejevs, A. Brantov, V.Y. Bychenkov, Experimental and theoretical study of absorption of femtosecond laser pulses in interaction with solid copper targets. Phys. Rev. B **79**, 144120 (2009)
71. A. Vorobyev, C. Guo, Enhanced energy coupling in femtosecond laser-metal interactions at high intensities. Opt. Express **14**, 13113–13119 (2006)
72. N. Bulgakova, V. Zhukov, A. Vorobyev, C. Guo, Modeling of residual thermal effect in femtosecond laser ablation of metals: Role of a gas environment. Appl. Phys. A **92**, 883–889 (2008)
73. N.M. Bulgakova, A.B. Evtushenko, Y.G. Shukhov, S.I. Kudryashov, A.V. Bulgakov, Role of laser-induced plasma in ultradeep drilling of materials by nanosecond laser pulses. Appl. Surf. Sci. **257**, 10876–10882 (2011)
74. A.Y. Vorobyev, I. Dorofeev, M. Libenson, Concerning the chemical source of energy in a laser flare. Sov. Tech. Phys. Lett. **18**, 172–173 (1992)